High Resolution and Multidimensional Protein Condensate Phase Diagrams with a Combinatorial Microdroplet Platform

William E. Arter,[1,†] Runzhang Qi,[1,†] Nadia A. Erkamp,[1,†] Georg Krainer,[1,†] Kieran Didi,[1] Timothy J. Welsh,[1] Julia Acker,[2] Jonathan Nixon-Abell,[3] Seema Qamar,[3] Yufan Xu,[1] Jordina Guillén-Boixet,[4] Titus M. Franzmann,[4] David Kuster,[5] Anthony A. Hyman,[5] Alexander Borodavka,[2] Peter St George-Hyslop,[3,6,7] Simon Alberti[4] and Tuomas P.J. Knowles[1,8,*]

[1] *Yusuf Hamied Department of Chemistry, Centre for Misfolding Diseases, University of Cambridge, Lensfield Road, Cambridge, CB2 1EW, UK*

[2] *Department of Biochemistry, University of Cambridge, Cambridge, CB2 1QW, UK*

[3] *Cambridge Institute for Medical Research, Department of Clinical Neurosciences, University of Cambridge, Cambridge CB2 0XY, UK*

[4] *Biotechnology Center (BIOTEC), Center for Molecular and Cellular Bioengineering (CMCB), Technische Universität Dresden, Tatzberg 47/49, 01307 Dresden, Germany*

[5] *Max Planck Institute for Molecular Cell Biology and Genetics, Pfotenhauerstrasse 108, 01307 Dresden, Germany*

[6] *Department of Medicine (Division of Neurology), University of Toronto and University Health Network, Toronto, Ontario M5S 3H2, Canada*

[7] *Department of Neurology, Columbia University, 630 West 168th St , New York, NY 10032, USA.*

[8] *Cavendish Laboratory, Department of Physics, University of Cambridge, J J Thomson Ave, Cambridge, CB3 0HE, UK*

[†] These authors contributed equally.

* To whom correspondence should be addressed:
E-mail: tpjk2@cam.ac.uk

Abstract

The assembly of intracellular proteins into biomolecular condensates through phase separation is a fundamental process underlying organisation of the intracellular space and regulation of many central cellular processes. Elucidating the physico-chemical parameters that modulate phase separation is crucial in order to understand its effects in health and disease, as well as to develop therapeutic strategies that target biomolecular condensate systems. Phase behaviour is described by the phase diagram that defines conditions at which distinct phases exist, as well as the boundaries between these phases. Phase diagrams are typically built up from numerous individual measurements sampling different parts of the phase space. For biomolecular condensates, this process is slow, low throughput and associated with significant sample consumption even when performed in microwell format. Due to the rapidly increasing number of biologically and disease-relevant condensate systems, experimental techniques that enable high-throughput analysis of protein phase behaviour are required. To address this challenge, we present here a combinatorial droplet microfluidic platform, termed PhaseScan, for the rapid and high-resolution acquisition of protein phase diagrams in multiple chemical and physical dimensions. Using this platform, we characterise the phase behaviour of a wide range of protein systems under a variety of conditions and show that this platform can be used to characterise quantitatively the effect of small molecules on biomolecular phase transitions.

Introduction

Many cellular proteins have the ability to demix into a protein-rich liquid condensate phase and a protein-depleted diluted phase.[1] This liquid–liquid phase separation (LLPS) process, has emerged as a fundamental mechanism to describe the formation of biological condensates in living cells.[2] Condensates systems such as stress granules, paraspeckles, and nuclear bodies are formed by LLPS and compartmentalise cellular space.[3] They act as microreactors for biochemical reactions,[4] and are crucial to a wide range of physiological processes such as gene expression, signalling, and metabolic regulation.[5–7] Condensate forming proteins are also heavily implicated in protein misfolding diseases including motor neuron disease,[8–10] cancer pathogenesis[11] and infectious diseases,[12] thus making them attractive targets for therapeutic intervention.[13,14]

Phase separation, now established for hundreds of cellular proteins,[15] can be triggered by variations in environmental conditions such as changes in ionic strength, pH, temperature, molecular crowding, and the presence of small molecules.[16–21] Because of this sensitivity to physicochemical parameters, there is great potential to modulate protein phase separation in a targeted manner and many phase separating proteins and their complexes are receiving intense interest as fundamentally novel drug targets to ameliorate human diseases.[22,23] However, it remains challenging to quantify the physical parameters that modulate phase separation behaviour in LLPS systems with high fidelity, accuracy and throughput.[16]

A central concept that characterises phase-separating systems is the phase diagram.[23–25] Phase diagrams summarise the phase behaviour of condensates by monitoring the position of the transition between the phase-separated and the mixed regimes through determination of the position of the phase boundary in chemical space.[26] Changes in the phase boundary for an LLPS system following variation of solution conditions affords insights to the thermodynamic processes driving protein condensation and the factors that modulate them.[17]

However, given the large variety of proteins undergoing LLPS and the environmental conditions which regulate their behaviour, there is a need for experimental methods that enable rapid and high-resolution characterisation of LLPS phase diagrams. Typically, these are generated by labour and time intensive methods involving the stepwise combination of reagents to create the requisite variation in solution conditions before observation of individual conditions by microscopy. Notably, although phase diagrams are often used to probe the

behaviour of LLPS systems, such experiments can only provide a coarse-grained picture of the protein phase-space when conducted manually.[27,28]

To address this challenge, we describe here a droplet microfluidic approach, PhaseScan, that enables rapid, automated generation of different LLPS solution conditions for high-resolution assessment of protein LLPS behaviour. Lab-on-a-chip microfluidic systems, in particular microdroplet-based formats, offer an effective means to improve assay throughput, parallelisation, and miniaturisation in biochemical experiments. To date these platforms have been leveraged to probe protein phase behaviour [29–31] by concentration or evaporation of dilute, homogeneous protein solutions contained in microdroplets, so that the system becomes sufficiently concentrated to pass into the phase-separated regime. Initiating phase separation by concentrating the solution means that salt and buffer are also concentrated, making it challenging to probe phase diagrams under fully physiological conditions or to map out phase diagrams in different independent chemical or physical diemnsions.

We aim to overcome these challenges through combinatorial droplet microfluidics to rapidly generate a large number of micro-compartments, each of which can be considered a discrete environment to study protein LLPS. By altering the input solution conditions, a broad range of phase separation environments are produced rapidly in order to map LLPS behaviour over chemical space. We demonstrate the operation of the PhaseScan platform by acquiring phase diagrams for a variety of phase-separating proteins and their modulation by molecular crowding, salt concentration, and nucleic acid concentration. We then investigate and compare the effect of small molecules on the protein phase separation. Finally, we show the acquisition of a three-dimensional phase diagram, demonstrating the potential of our platform for parallelised, multi-dimensional analysis of chemical space in the context of protein phase separation.

Results and Discussion

Working principle of the PhaseScan platform

First, we implemented a workflow for microdroplet generation and imaging (Figure 1(a)). As a model system to establish the workflow, we utilised an EGFP-tagged G156E mutant of the protein fused in sarcoma (FUS^{G156E}), a protein implicated in the pathology of amyotrophic lateral sclerosis (ALS) via an aberrant phase-separation mechanism.[9,10] Phase separation was triggered by molecular crowding with polyethylene glycol (PEG), as reported previously.[9]

Figure 1: PhaseScan workflow.

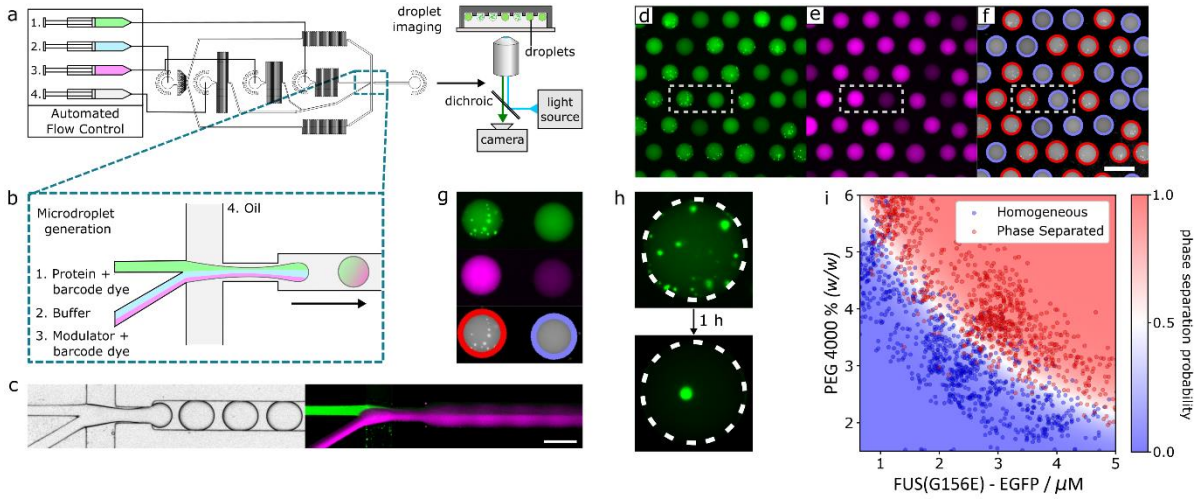

(a) Droplets are generated using a flow-focussing microfluidic device controlled by automated syringe pumps and then imaged in wells by fluorescence microscopy. **(b)** At the droplet generating junction, aqueous solutions are combined under laminar flow before droplet formation. **(c)** Brightfield microscopy image of droplet generation (left) and combined fluorescence images of droplet generation (right) showing fluorescence of EGFP (green) and Alexa647 (magenta) barcodes for FUS^{G156E} and PEG, respectively. **(d, e)** Epifluorescence microscopy images of trapped microdroplets, with EGFP and Alexa647 fluorescence corresponding to FUS^{G156E} and PEG concentration, respectively. **(f)** Classification of droplets as phase separated (red outline) or homogeneous (blue outline) according to distribution of EGFP fluorescence. **(g)** Phase separated (left) and homogeneous (right) microdroplets imaged according to EGFP (top) and Alexa647 fluorescence (middle) and subsequent phase separation classification (bottom). Images correspond to the highlighted regions in (d-f). **(h)** Liquid condensates merge over time in microdroplets. **(i)** Phase diagram of EGFP-FUS^{G156E} vs. PEG 4000 concentration, 50 mM Tris pH 7.4, 150 mM KCl. Red and blue data points in the scatter plot correspond to individual phase separated or homogeneous droplets, respectively. The heat map corresponds to the probability of phase separation as determined by an SVM classifier trained on the droplet scatter plot.

Aqueous solutions containing protein, buffer, and the modulator PEG were mixed in different ratios on chip prior to encapsulation in water-in-oil microcompartments of ~700 pL in volume dispersed inan immiscible fluorinated-oil continuous phase (Figure 1(b)). Due to laminar flow, the aqueous solutions do not mix significantly before droplet formation,[32] and

droplet coalescence is prevented by supplementing the fluorinated oil phase with a biologically compatible polyglycerol-based triblock surfactant (see Methods).[33] The relative flow rates of the aqueous solutions are altered while the total flow rate is kept constant using a programme controlled by an automated syringe pump system. This enables the formation of droplets containing protein and PEG concentrations over a range of chemical space. To determine the amount of protein and PEG present in each droplet in downstream analysis, the concentration of each of these components was barcoded by a particular fluorophore (Figure 1(b, c)). For FUS^{G156E}, this information was provided by its EGFP tag, whereas the concentration of PEG was barcoded by Alexa647 dye pre-mixed into the PEG starting solution (see Methods).

Following generation, droplets were collected in a PDMS gravity-trap device, that utilises the lower density of droplets in comparison to the surrounding oil to immobilise droplets in microwells contained in the roof of a flow chamber, as described previously.[29,34] Approximately 2600 droplets were collected per experiment, with droplet generation occurring over a timescale that allowed at least two repetitions of the flow programme to ensure that the full range of conditions were scanned, before undergoing epifluorescence microscopy imaging according to the fluorescence wavelengths of each of the barcode fluorophores (Figure 1(d, e)). According to the barcode fluorescence intensity, the corresponding concentrations of protein or PEG were determined on a per-droplet basis by comparison to a calibration measurement of known fluorophore concentration (see Methods).

Droplets were then classified as phase-separated or homogeneous according to the presence or absence of condensates, visualised via the protein EGFP tag. Figure 1(g, f) demonstrate the assignment for a representative image of phase-separated and homogeneous droplets containing EGFP-FUS^{G156E}, with a red or blue outline indicating classification of droplets as phase separated or homogeneous, respectively. We observed merging of condensates over time (Figure 1h), which together with off-chip fluorescence recovery after photobleaching (FRAP) experiments (Supporting Information, Figure S1) confirmed the liquid nature of condensates formed in the PhaseScan experiment. By combining the determined concentration and the presence or absence of phase separation as a scatter plot on a per-droplet basis, a phase diagram was produced (Figure 1(i)). The position of the phase boundary and probability of phase separation as a function of EGFP-FUS^{G156E} and PEG concentration was then determined by a support-vector machine (SVM) algorithm trained on the scatter-plot populations of phase-separated or homogeneous droplets (Figure 1(i), see Methods). Notably, only a technique with

sufficient throughput allows the use of statistical methods to comprehensively and continuously describe phase space in the manner demonstrated here.

We observe that droplets can be classified robustly into phase separated or homogeneous regions according to concentrations of FUS^{G156E} and PEG that show excellent agreement with previous studies.[9] The homotypic phase separation of wild-type EGFP-FUS was also assessed and similar behaviour was observed (data not shown). To assess whether the phase-behaviour of FUS^{G156E} was notably altered by droplet encapsulation, the presence or absence of phase separation under the same conditions as those probed by PhaseScan were confirmed as the same in bulk volumes by manual pipetting experiments (Supporting Information, Figure S2). Importantly, although the phase-separation systems described herein are characterised by use of fluorophore-tagged proteins, this is not a pre-requisite for operation of the PhaseScan platform as the presence of condensates within droplets could instead be observed by brightfield microscopy as shown elsewhere[29,35] and in Figure S1.

To test whether the barcoding dyes affect the phase boundary, the phase behaviour of FUS^{G156E} was assessed as a function of Alexa546 and Alexa647 dye concentration (Supporting Information, Figure S3). No significant effect was observed, with phase separation propensity remaining unchanged for the barcode concentrations used here (< 6.5 μM, see Methods).

We also investigated the potential for droplet size to effect the reported position of the phase boundary, since droplet volume has the propensity to modulate the dynamics of nucleation-driven condensate growth.[36] Phase diagrams for homotypic FUS^{G156E} condensates were recorded using droplets of two different sizes with mean volumes of 0.33 and 1.1 nL, which bracketed the typical droplet volume of 0.65 nL used in PhaseScan experiments (Supporting Information, Figure S4). No difference was observed between these phase diagrams, indicating that the experimental timescales employed here, with several minutes between droplet generation and imaging, render the experiment insensitive to droplet volume.

For the PhaseScan experiment to be a useful analytical tool with which to investigate protein phase behaviour, it is imperative that phase diagrams can be reproducibly generated. To demonstrate that this is the case, phase diagrams for homotypic FUS^{G156E} phase separation were produced in triplicate from three independent experiments (Supporting Information, Figure S5). Only negligible differences were observed between the analyses, demonstrating that the PhaseScan approach can robustly characterise phase separation behaviour.

Notably, the PhaseScan technique provides throughput several orders of magnitude higher than manual experiments in terms of the number of unique conditions investigated, with >2500 droplets assayed per experiment. Reagent consumption is minimal, with < 2 μL of stock protein solution used per assay, although we found that a minimum working volume of 10 μL was required for effective operation (see Methods). Moreover, data generation is rapid, with droplet generation and collection requiring approximately 5 min. This is in contrast to microfluidic approaches for investigation of LLPS based on droplet shrinking, which can require experimental timescales of several hours.

PhaseScan is generalisable to a range of phase-separating systems

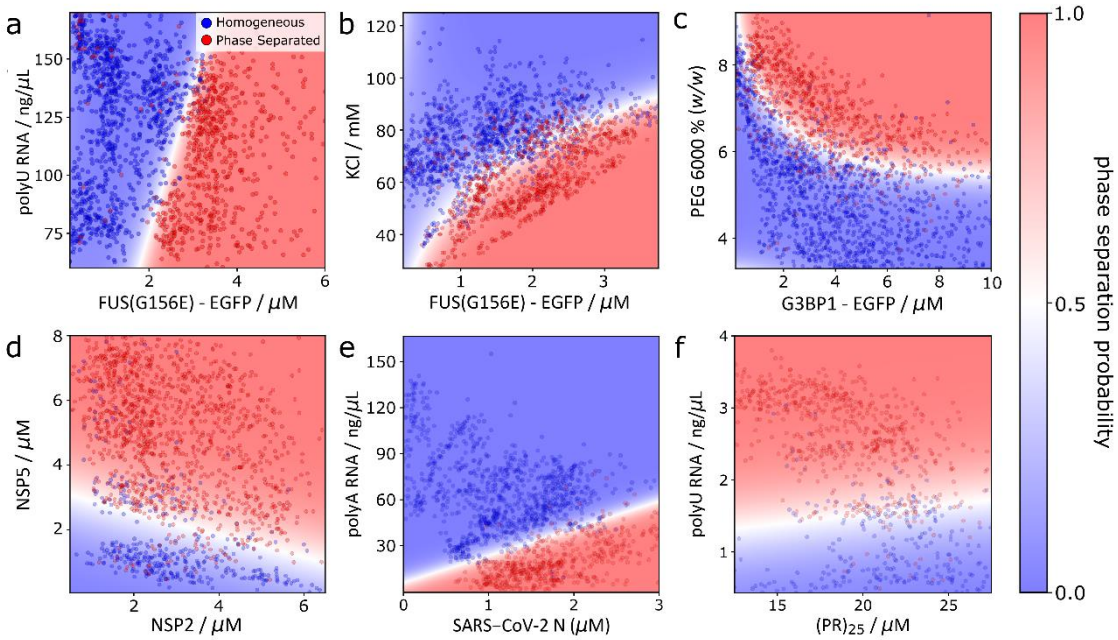

Figure 2: Application of PhaseScan to a variety of condensate systems. (a) Phase diagram of EGFP-tagged FUS^{G156E} vs. polyU RNA concentration. **(b)** Phase diagram of FUS^{G156E} condensation as a function of protein and salt concentration. **(c)** Phase diagram of EGFP-tagged G3BP1 vs. PEG 6000 concentration. **(d)** Phase diagram for coacervation-condensation of rotavirus proteins NSP2 and NSP5. **(e)** Phase diagram for polyA RNA-mediated phase separation of SARS-CoV-2 N protein. **(f)** Phase diagram for polyU RNA-mediated phase separation of the dipeptide repeat $(PR)_{25}$.

Having validated the operation of the PhaseScan system, we then sought to utilise our platform for the investigation of a range of phase-separating systems and test the generality of the method for homotypic and heterotypic condensate systems.

Since coacervation of nucleic acids is a defining characteristic of phase-separated ribonucleoprotein granules, we began by producing a phase diagram for condensation of EGFP-tagged FUS^{G156E} in the presence of polyU RNA (Figure 2(a)). As observed previously,[37]

no phase separation was detected at low ratios of FUS^{G156E} relative to RNA, with phase-separation then occurring at higher FUS^{G156E} concentrations. Notably, the phase boundary appears highly linear, in agreement with studies that suggest that condensate formation and protein–RNA coacervation occurs via charge neutralisation,[37] and that condensation therefore occurs at a discrete ratio of RNA to protein.

Next, we generated a phase diagram for the phase separation of FUS^{G156E} as a function of KCl concentration (Figure 2(b)). In agreement with previous findings, FUS^{G156E} was observed to possess an increased propensity for phase separation at high protein and low salt concentrations. Analysis of the effect of ionic strength on the propensity of condensate systems to phase separate can afford mechanistic insight into the molecular-level interactions that drive LLPS, by elucidating the extent to which phase separation, for example, is influenced by electrostatic interactions.[38,39] We therefore envisage that PhaseScan could enable rapid, high-resolution mechanistic analysis of phase separation processes.

To demonstrate the applicability of the PhaseScan system to further phase separating proteins, we next characterised the crowding-driven phase separation of EGFP-tagged G3BP1, a scaffolding protein required for the formation of stress granules (Figure 2(c)).[40] As expected, phase separation of G3BP1 was present at high concentrations of PEG molecular crowder, with this effect enhanced at higher protein concentration.

We then assayed the formation of phase separated protein–protein coacervates by investigating the condensation of rotavirus proteins NSP2 and NSP5 (Figure 2(d)). These proteins are key constituents of membraneless viral replication factories known as the viroplasm; recent studies suggest that LLPS provides a mechanism for viroplasm construction.[41,42] In agreement with these findings, and in support of a recent study demonstrating coacervation of NSP2 and NSP5 both in vivo and in vitro,[43] we observe condensation of NSP2 and NSP5 in a concentration-dependent manner, with an NSP2-dependent threshold of NSP5 relative to NSP2 required for LLPS to occur.

In addition, we probed phase separation of the nucleocapsid protein of the human coronavirus SARS-CoV-2 (SARS-CoV-2 N) (Figure 2(e)). In accordance with previous findings,[44,45] we observe phase separation in an RNA-dependent manner. The ordinarily homogeneous SARS-CoV-2 N protein phase separated in the presence of polyA RNA concentrations below 25 ng/μL, however no phase separation was visible at RNA concentration above 65 ng/μL. The exact position of the phase boundary varied according to SARS-CoV-2

N concentration, with a higher protein concentration requiring a correspondingly higher concentration of RNA for phase separation to be ablated. These results are in agreement with previous studies, which have shown through manual experiments that phase separation of SARS-CoV-2 N can be driven by the presence of RNA, but that excess nucleic acid concentrations result in condensate dissolution.[45]

Finally, we examined the phase behaviour of a dipeptide repeat system derived from the hexanucleotide repeat expansion in the chromosome 9 open reading frame 72 (C9orf72) gene, implicated in ALS.[46] The peptide consisted of 25 repeats of proline–arginine dipeptide $(PR)_{25}$. This type of peptide is well known to phase separate when mixed with negatively charged polymers, including single-stranded RNA. Using PhaseScan, we assayed the formation of $(PR)_{25}$ with poly uridine ($PolyU_{100}$) RNA (Figure 2(f)), and observed RNA-dependent phase separation above 1.5 ng/μL RNA for ~20 μM $(PR)_{25}$.

In summary, these experiments demonstrate that the PhaseScan approach is applicable to a broad range of condensate systems, including homo- and heterotypic phase separation of full-length proteins, protein-RNA and protein-protein coacervates, and simple peptide systems.

Observation of small-molecule modulation of phase separation

Next, we applied our platform to the investigation of the effect of small molecules on phase separation. There is great interest in identifying compounds that modulate LLPS as condensate forming processes are associated with a wide range of diseases, including neurodegenerative disorders and cancer.[14,47–49] Critical to this effort is the provision of high-resolution phase diagrams for the accurate quantification of the effect of small-molecule modulators on the phase separation equilibrium. Moreover, for high-throughput screening of drug candidates, it is imperative that the phase diagram for a particular drug–protein combination is acquired rapidly. The PhaseScan platform brings together these features and enables fast, automated generation of different LLPS solution conditions for high-resolution assessment of changes in protein LLPS behaviour.

To establish the applicability of the PhaseScan system for probing the effects of small-molecule compounds, we first determined the modulation of FUS^{G156E} phase separation by the small molecule 4,4′-dianilino-1,1′-binaphthyl-5,5′-disulfonic acid (bis-ANS), a compound which has recently been shown to act as a potent modulator of various phase separating proteins, including the FUS low-complexity domain.[49] To this end, we modified the microdroplet generator to allow the addition of a fourth solution component to the PhaseScan

experiment (Figure S6), which in this case contained the small-molecule modulator bis-ANS. This solution was injected into the PhaseScan experiment at a constant flowrate, in addition to EGFP-tagged FUS^{G156E}, PEG and buffer solutions at varying flow rates, to achieve an equal concentration of the small molecule in each droplet (see Methods). Bis-ANS was at a concentration of 1 mM (in 1% DMSO) and was diluted 10-fold on chip to results in a final concentration of 100 µM (0.1% DMSO) in the droplet. As a control, we performed an experiment without bis-ANS but with buffer supplemented with 1% DMSO (i.e., 0.1 % DMSO in the droplet). As shown in Figure 3(a, b), the position of the phase boundary shifted markedly towards lower protein and lower PEG concentrations in the presence of bis-ANS, in line with previous observations on the LCD of FUS.[49] A differential map of the SVM-derived heat maps quantifies the shift of the phase boundary (Figure 3(c)), thus providing a means to quantitatively assess the effect of chemical modulators on phase behaviour.

In summary, the PhaseScan approach provides a high-resolution assessment of changes in protein LLPS behaviour upon small-molecule addition. This feature is significant, as the effect of many candidate molecules is likely to be subtle, and identification of potential hits from a naïve candidate panel would require high assay resolution. PhaseScan achieves this rapidly with minimal sample consumption, promising efficient scale-up for high-content library screening.

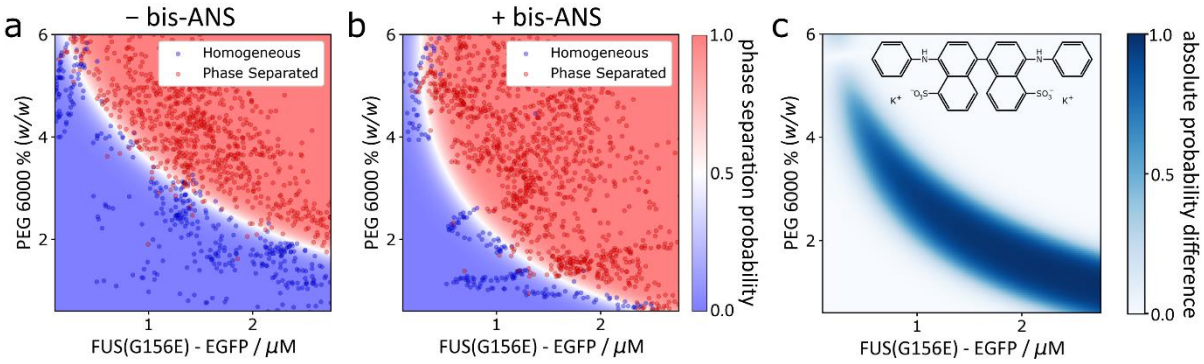

Figure 3: Probing the effect of small molecule modulators on phase separation using PhaseScan. (a) Control phase diagram of EGFP-tagged EGFP-tagged FUS^{G156E} vs. PEG 6000 concentration in the absence of bis-ANS. **(b)** Phase diagram of EGFP-tagged EGFP-tagged FUS^{G156E} vs. PEG 6000 concentration in the presence of bis-ANS **(c)** Molecular structure of bis-ANS and differential phase diagram of homotypic FUS phase diagram ± bis-ANS.

Generation of multi-dimensional phase diagrams

It has been established that a variety of environmental factors can trigger or modulate LLPS, a factor that underlies their versatility in terms of the biological functions that they fulfil. Investigation of these effects is typically constrained to analysis in two-dimensional (2D) chemical space, primarily due to the impractically large number of individual experiments that must be carried out if multiple parameters are investigated simultaneously by manual methods. Since the PhaseScan platform enables automated and high-throughput generation of a wide range of solution conditions, we sought to expand the platform to enable investigation of multi-dimensional chemical space beyond conventional two dimensional phase diagrams in a single experiment, including small-molecule modulation.

To demonstrate this, we performed a three-dimensional (3D) parameter space PhaseScan experiment on FUS^{G156E}. We included 1,6-hexanediol (1,6-HD), a small molecules known to interfere with LLPS behaviour that has been employed extensively to probe LLPS systems.[19] This was added as a fourth component to the PhaseScan mix in addition to EGFP-tagged FUS^{G156E}, PEG and buffer solutions (Figure S6). Following droplet generation, trapping and imaging (~7500 droplets), the relative concentrations of each of the three barcodes was used to determine the concentrations of FUS^{G156E}, PEG and 1,6-HD present in each drop. This measurement was combined with the classification of each droplet as containing phase separated or homogeneous protein to construct a three-dimensional phase diagram for the system (Figure 4(a, b), Supporting Movie 1). As before, the concentration of EGFP-tagged FUS^{G156E} and PEG were barcoded by the EGFP tag and the addition of Alexa647 dye, respectively, whereas the concentration of 1,6-HD was barcoded by the addition of Alexa546 (Figure 4(c)).

As observed in the 2D phase diagrams shown previously, and evident in the projection from the 3D phase diagrams (Figure 4(d–f)), phase separation was favoured at high protein and PEG concentrations. As expected, phase separation was reduced at higher concentrations of 1,6-HD, since 1,6-HD is known in disrupt protein condensation by competing for hydrophobic interactions that commonly drive protein LLPS. Notably, the antagonistic effects of molecular crowding and 1,6-HD on phase separation as a function of protein concentration are simultaneously observable (Figure 4(e–g)). We propose that the ability to assess multiple modulators of phase separation in a single experiment presents a facile, high-resolution means with which to investigate mechanistic aspects of phase separation with minimal sample consumption (<6 μL of protein solution).

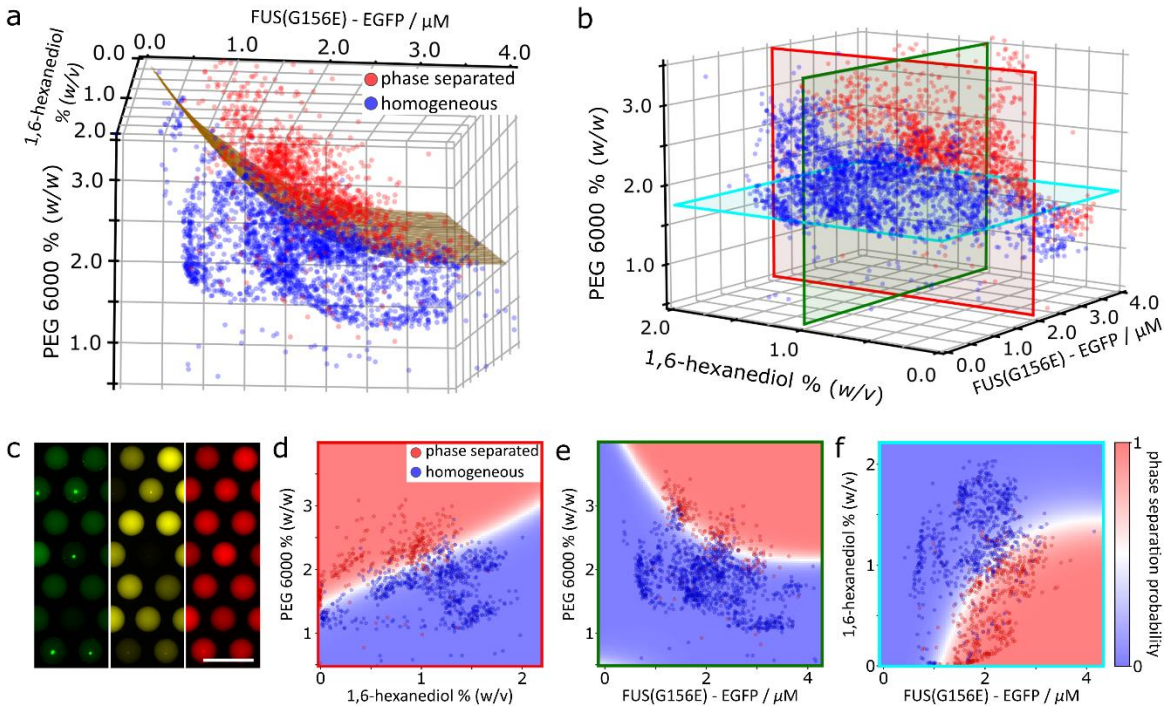

Figure 4: Generation of multidimensional phase diagrams using the PhaseScan platform. (a, b) 3D phase diagram of EGFP-tagged FUS^{G156E} vs. PEG 6000 vs. 1,6-HD concentration. **(c)** Epifluorescence microscopy images of trapped microdroplets with EGFP (green), Alexa546 (yellow), and Alexa647 (red) fluorescence corresponding to FUS^{G156E} and 1,6-HD, and PEG concentrations, respectively. **(d-f)** 2D slices of the 3D phase diagram, corresponding to the red, green and blue planes shown in (b), respectively.

Conclusions

Biomolecular condensation has transformed our understanding of cell biology. Physicochemical characterisation of the parameters that control and modulate phase separation has thus become essential for an improved understanding of protein phase behaviour, including for the therapeutic modulation of LLPS phenomena. The PhaseScan platform presented herein provides a basis for the rapid and high-resolution acquisition of LLPS phase diagrams through the application of microdroplet techniques. We have demonstrated that the PhaseScan approach is applicable to a wide range of phase-separating systems ranging from coacervating peptides, human proteins and viral proteins, and provides a useful tool to enable rapid, high-resolution mechanistic analysis of phase separation processes. PhaseScan further enables the provision of high-resolution phase diagrams for the accurate quantification of the effect of small molecule modulators on the phase separation equilibrium, a feature that is essential in drug screening efforts. Uniquely, PhaseScan allows exploration of higher-dimensional chemical space in a single experiment, including the effect of small-molecule modulation, with minimal sample consumption.

We envisage that microfluidic platforms such as those presented here can find many applications in the quantitation of LLPS equilibria, such as, for example, the screening of candidate small molecules for the therapeutic modulation of phase-separation behaviour. Future work could utilise a combination of the PhaseScan and droplet-shrinking approaches,[29] whereby an initial library of droplets are produced that possess a variety of chemical conditions, before these droplets are then shrunk by evaporation. Thus, the concentration-driven onset of LLPS could be assessed in a highly parallelised manner given the large number of unique starting conditions. Indeed, we have acquired proof-of-concept of this approach via shrinkage of droplets containing a range of FUS156 and RNA concentrations (Supporting Information, Figure S7). Moreover, together with methods for rapid auto-sampling of different drug–protein combinations (e.g., robotic microinjectors/autopipettes) and improved optics, faster assay speed and lower sample consumption can be achieved. We note that with the relatively low droplet generation rate we employ here (~30 Hz), future experiments could achieve an improved assay throughput by integrating the droplet-microscopy step with high frequency droplet generation. This approach opens up a route towards exploration of the phase space of proteins and nucleic acids at high resolution and high throughput.

Materials and Methods

Materials

All reagents and chemicals were purchased with the highest purity available. Tris as a buffer reagent and KCl were from Fisher Scientific. PolyU and PolyA RNA with a molecular weight range from 800–1000 kDa was purchased from Sigma Aldrich as lyophilized powder. $PolyU_{100}$ RNA was purchased from Biomers as lyophilized power and dissolved into a stock of 1 mg/mL in mQ water before use 1,6-HD was purchased from Santa Cruz Biotechnology. Bis-ANS was purchased from Invitrogen and dissolved to make a stock solution in DMSO (Sigma Aldrich). Alexa546 and Alexa647 carboxylic acid were obtained from Thermo Fisher. PEG 4000 and 6000 were from Sigma Aldrich. Details on the production of proteins (FUS^{G156E}-EGFP, G3BP1-GFP, NSP2/5, SARS-CoV-2 N and $(PR)_{25}$ are given in the Supporting Information.

Device fabrication

PDMS (Corning) devices for droplet generation and multilayer well-devices for droplet collection and imaging were produced on SU-8 (Microchem) moulds fabricated via photolithographic processes as described previously.[50–52] Further details are provided in the Supporting Information.

Droplet generation

Syringe pumps (neMESYS modules, Cetoni) were used to control flows of protein, buffer and LLPS trigger supplemented with barcoding dyes as appropriate. The aqueous flowrates were configured to vary automatically according to pre-set gradients, with constant total flow rate of 60 μL/h, to scan phase space over a nominal concentration range of approximately one order of magnitude for each of the component solutions. FC-40 oil (containing 1.5% (*v*/*v*) fluorosurfactant, RAN Biotechnologies) was introduced to the device at a constant flow rate of 50–120 μL/h for generation of microdroplets of approximately 650 pL volume. Droplets were trapped in a floating droplet array[34] directly after generation. For further details see Supporting Information.

Imaging

Trapped microdroplets were imaged using an AxioObserver D1 microscope (Zeiss) equipped with a 5x air objective (Zeiss) and a high-sensitivity camera (Evolve 512, Photometrics). Appropriate filter sets were used for EFGP, Alexa Fluor 546 and Alexa Fluor 647 detection (Chroma Technology 49002, 49004 and 49006, respectively). Minimal crosstalk between fluorescence channels was observed, which was removed during the image processing and calibration procedure (see Supporting Information, Figure S8).

Droplet detection and phase diagram generation

Acquired images were analysed using a custom-written Python script. Representative data and additional details are provided in the Supporting Information (Figures S8 and S9). Briefly, droplets were fitted as circles in the images. Non-circular droplets or erroneous detections were filtered and removed. From the fitted circular areas, the total intensity was calculated and normalised to obtain the intensity per unit volume (calculated using the fitted diameter), and converted to concentrations by comparison to calibration images acquired with known barcode concentration (Figure S8). Droplets were classified as phase-separated or homogeneous according to the presence or absence of at least three connected pixels of an intensity above an algorithm-defined threshold intensity. Representative classification output is presented in the Supporting Information (Figure S8). Droplet classification and barcode concentrations were then combined on a per-droplet basis to produce phase diagrams. A Support Vector Machine algorithm was then trained on the droplet dataset to produce a probability map of phase separation over the phase-space in question.

Acknowledgements

The research leading to these results has received funding from the EPSRC (award RG90413, W.E.A.), a Royall Scholarship (N.A.E.), a Krishnan-Ang Studentship (R.Q.), Trinity College (Cambridge Honorary Trinity-Henry Barlow Scholarship; R.Q.), the Cambridge Trust (Honorary International Scholarship; R.Q.), the European Research Council under the European Union's Horizon 2020 Framework Programme through the Marie Skłodowska-Curie grant MicroSPARK (agreement no. 841466; G.K.), the Herchel Smith Fund of the University of Cambridge (G.K.), the Wolfson College Junior Research Fellowship (G.K.), the Winston Churchill Foundation of the United States (T.J.W.), the Harding Distinguished Postgraduate Scholar Programme (T.J.W.), the Wellcome Trust Henry Wellcome fellowship 218651/Z/19/Z (J.N.A), the Wellcome Trust [213437/Z/18/Z] (A. B), the Canadian Institutes of Health Research (Foundation Grant and Canadian Consortium on Neurodegeneration in Aging Grant) (P.StGH.), US Alzheimer Society Zenith Grant ZEN-18-529769 (P.StGH.), Alzheimer Society of Ontario Chair in Alzheimer's Disease Research (P.StGH), a Wellcome Trust Collaborative Award 203249/Z/16/Z (P.StGH, T.P.J.K.), the European Research Council under the European Union's Seventh Framework Programme (FP7/2007-2013) through the ERC grants PhysProt (agreement no. 337969; T.P.J.K.) and the Newman Foundation (T.P.J.K.).

Author Contributions

W.E.A., G.K., and T.P.J.K. conceived the study. W.E.A., N.A.E., R.Q., K.D., T.J.W., J.A., J. N.-A. and Y.X. performed experiments. R.Q. and W.E.A. developed analytical tools. T.M.F., J.G.-B., A.B., D.K., S.A., and P.St.G.-H. provided materials. W.E.A. and G.K. wrote the original draft, all authors reviewed and edited the paper.

Conflict of interest

Parts of this work have been the subject of a patent application filed by Cambridge Enterprise Limited, a fully owned subsidiary of the University of Cambridge. T.P.J.K. and P. StGH. are founders, and W.E.A. and G.K. are employees of Transition Bio Ltd.

References

1. Boeynaems, S. *et al.* Protein Phase Separation: A New Phase in Cell Biology. *Trends Cell Biol.* **28**, 420–435 (2018).

2. Hyman, A. A., Weber, C. A. & Jülicher, F. Liquid-Liquid Phase Separation in Biology.

Annu. Rev. Cell Dev. Biol. **30**, 39–58 (2014).

3. Shin, Y. & Brangwynne, C. P. Liquid Phase Condensation in Cell Physiology and Disease. *Science* vol. 357 (2017).

4. Banani, S. F., Lee, H. O., Hyman, A. A. & Rosen, M. K. Biomolecular Condensates: Organizers of Cellular Biochemistry. *Nature Reviews Molecular Cell Biology* vol. 18 285–298 (2017).

5. Sokolova, E. *et al.* Enhanced Transcription Rates in Membrane-Free Protocells Formed by Coacervation of Cell Lysate. *Proc. Natl. Acad. Sci. U. S. A.* **110**, 11692–11697 (2013).

6. Kim, T. H. *et al.* Phospho-Dependent Phase Separation of FMRP and CAPRIN1 Recapitulates Regulation of Translation and Deadenylation. *Science (80-.).* **365**, 825–829 (2019).

7. Riback, J. A. *et al.* Stress-Triggered Phase Separation Is an Adaptive, Evolutionarily Tuned Response. *Cell* **168**, 1028-1040.e19 (2017).

8. Boeynaems, S. *et al.* Phase Separation of C9orf72 Dipeptide Repeats Perturbs Stress Granule Dynamics. *Mol. Cell* **65**, 1044-1055.e5 (2017).

9. Patel, A. *et al.* A Liquid-to-Solid Phase Transition of the ALS Protein FUS Accelerated by Disease Mutation. *Cell* **162**, 1066–1077 (2015).

10. Murakami, T. *et al.* ALS/FTD Mutation-Induced Phase Transition of FUS Liquid Droplets and Reversible Hydrogels into Irreversible Hydrogels Impairs RNP Granule Function. *Neuron* **88**, 678–690 (2015).

11. Bouchard, J. J. *et al.* Cancer Mutations of the Tumor Suppressor SPOP Disrupt the Formation of Active, Phase-Separated Compartments. *Mol. Cell* **72**, 19-36.e8 (2018).

12. Geiger, F. *et al.* Rotavirus Replication Factories Are Complex Ribonucleoprotein Condensates. *bioRxiv* (2020) doi:10.1101/2020.12.18.423429.

13. Mullard, A. Biomolecular Condensates Pique Drug Discovery Curiosity. *Nat. Rev. Drug Discov.* (2019) doi:10.1038/d41573-019-00069-w.

14. Wheeler, R. J. *et al.* Small Molecules for Modulating Protein Driven Liquid-Liquid Phase Separation in Treating Neurodegenerative Disease. *bioRxiv* 721001 (2019) doi:10.1101/721001.

15. Li, Q. *et al.* LLPSDB: A Database of Proteins Undergoing Liquid-Liquid Phase Separation in Vitro. *Nucleic Acids Res.* **48**, D320–D327 (2020).

16. Alberti, S., Gladfelter, A. & Mittag, T. Considerations and Challenges in Studying Liquid-Liquid Phase Separation and Biomolecular Condensates. *Cell* **176**, 419–434 (2019).

17. Riback, J. A. *et al.* Composition-Dependent Thermodynamics of Intracellular Phase Separation. *Nature* 1–6 (2020) doi:10.1038/s41586-020-2256-2.

18. Braun, M. K. *et al.* Reentrant Phase Behavior in Protein Solutions Induced by Multivalent Salts: Strong Effect of Anions Cl - Versus NO 3-. *J. Phys. Chem. B* **122**, 11978–11985 (2018).

19. Kroschwald, S., Maharana, S. & Simon, A. Hexanediol: A Chemical Probe to Investigate the Material Properties of Membrane-Less Compartments. *Matters* (2017) doi:10.19185/matters.201702000010.

20. Nott, T. J., Craggs, T. D. & Baldwin, A. J. Membraneless organelles can melt nucleic acid duplexes and act as biomolecular filters. *Nat. Chem.* **8**, 569–575 (2016).

21. Nott, T. J. *et al.* Phase Transition of a Disordered Nuage Protein Generates Environmentally Responsive Membraneless Organelles. *Mol. Cell* **57**, 936–947 (2015).

22. Wheeler, R. J. Therapeutics—How to Treat Phase Separation-Associated Diseases. *Emerg. Top. Life Sci.* (2020) doi:10.1042/ETLS20190176.

23. Alberti, S. & Dormann, D. Liquid–Liquid Phase Separation in Disease. *Annu. Rev. Genet.* **53**, 171–194 (2019).

24. Klamser, J. U., Kapfer, S. C. & Krauth, W. Thermodynamic Phases in Two-Dimensional Active Matter. *Nat. Commun.* **9**, 5045 (2018).

25. Bracha, D. *et al.* Mapping Local and Global Liquid Phase Behavior in Living Cells Using Photo-Oligomerizable Seeds. *Cell* **175**, 1467-1480.e13 (2018).

26. Brangwynne, C. P., Tompa, P. & Pappu, R. V. Polymer Physics of Intracellular Phase Transitions. *Nat. Phys.* **11**, 899–904 (2015).

27. Yang, P. *et al.* G3BP1 Is a Tunable Switch that Triggers Phase Separation to Assemble Stress Granules. *Cell* **181**, 325-345.e28 (2020).

28. Peskett, T. R. *et al.* A Liquid to Solid Phase Transition Underlying Pathological

Huntingtin Exon1 Aggregation. *Mol. Cell* **70**, 588-601.e6 (2018).

29. Kopp, M. R. G. *et al.* Microfluidic Shrinking Droplet Concentrator for Analyte Detection and Phase Separation of Protein Solutions. *Anal. Chem.* **92**, 5803–5812 (2020).

30. Taylor, N. *et al.* Biophysical characterization of organelle-based RNA/protein liquid phases using microfluidics. *Soft Matter* **12**, 9142–9150 (2016).

31. Celetti, G. *et al.* The Liquid State of FG-Nucleoporins Mimics Permeability Barrier Properties of Nuclear Pore Complexes. *J. Cell Biol.* e201907157 (2020) doi:10.1083/jcb.201907157.

32. Song, H., Tice, J. D. & Ismagilov, R. F. A microfluidic system for controlling reaction networks in time. *Angew. Chemie - Int. Ed.* (2003) doi:10.1002/anie.200390203.

33. Agresti, J. J. *et al.* Ultrahigh-Throughput Screening in Drop-Based Microfluidics for Directed Evolution. *Proc. Natl. Acad. Sci. U. S. A.* **107**, 4004–9 (2010).

34. Labanieh, L., Nguyen, T. N., Zhao, W. & Kang, D. K. Floating droplet array: An ultrahigh-throughput device for droplet trapping, real-time analysis and recovery. *Micromachines* **6**, (2015).

35. Bremer, A., Mittag, T. & Heymann, M. Microfluidic characterization of macromolecular liquid–liquid phase separation. *Lab Chip* **20**, 4225–4234 (2020).

36. Linsenmeier, M. *et al.* Dynamics of Synthetic Membraneless Organelles in Microfluidic Droplets. *Angew. Chemie Int. Ed.* **58**, 14489–14494 (2019).

37. Banerjee, P. R., Milin, A. N., Moosa, M. M., Onuchic, P. L. & Deniz, A. A. Reentrant Phase Transition Drives Dynamic Substructure Formation in Ribonucleoprotein Droplets. *Angew. Chemie Int. Ed.* **56**, 11354–11359 (2017).

38. Krainer, G. *et al.* Reentrant liquid condensate phase of proteins is stabilized by hydrophobic and non-ionic interactions. *Nat. Commun. 2021 121* **12**, 1–14 (2021).

39. Wang, J. *et al.* A Molecular Grammar Governing the Driving Forces for Phase Separation of Prion-like RNA Binding Proteins. *Cell* **174**, 688-699.e16 (2018).

40. Guillén-Boixet, J. *et al.* RNA-Induced Conformational Switching and Clustering of G3BP Drive Stress Granule Assembly by Condensation. *Cell* **181**, 346-361.e17 (2020).

41. Nikolic, J. *et al.* Negri bodies are viral factories with properties of liquid organelles. *Nat.*

Commun. **8**, 1–12 (2017).

42. Guseva, S. *et al.* Measles virus nucleo- And phosphoproteins form liquid-like phase-separated compartments that promote nucleocapsid assembly. *Sci. Adv.* **6**, eaaz7095 (2020).

43. Geiger, F. *et al.* Liquid–liquid phase separation underpins the formation of replication factories in rotaviruses. *EMBO J.* e107711 (2021) doi:10.15252/EMBJ.2021107711.

44. Perdikari, T. M. *et al.* SARS-CoV-2 nucleocapsid protein phase-separates with RNA and with human hnRNPs. *EMBO J.* **39**, (2020).

45. Lu, S. *et al.* The SARS-CoV-2 nucleocapsid phosphoprotein forms mutually exclusive condensates with RNA and the membrane-associated M protein. *Nat. Commun.* **12**, (2021).

46. Van Blitterswijk, M., Dejesus-Hernandez, M. & Rademakers, R. How do C9ORF72 repeat expansions cause amyotrophic lateral sclerosis and frontotemporal dementia: Can we learn from other noncoding repeat expansion disorders? *Curr. Opin. Neurol.* **25**, 689–700 (2012).

47. Dolgin, E. Drug startups coalesce around condensates. *Nat. Biotechnol.* **39**, 123–125 (2021).

48. Klein, I. A. *et al.* Partitioning of cancer therapeutics in nuclear condensates. *Science (80-.).* **368**, 1386–1392 (2020).

49. Babinchak, W. M. *et al.* Small molecules as potent biphasic modulators of protein liquid-liquid phase separation. *Nat. Commun.* **11**, (2020).

50. McDonald, J. C. *et al.* Fabrication of Microfluidic Systems in Poly(dimethylsiloxane). *Electrophoresis* **21**, 27–40 (2000).

51. Arter, W. E. *et al.* Digital Sensing and Molecular Computation by an Enzyme-Free DNA Circuit. *ACS Nano* (2020) doi:10.1021/acsnano.0c00628.

52. Mazutis, L. *et al.* Single-Cell Analysis and Sorting Using Droplet-Based Microfluidics. *Nat. Protoc.* **8**, 870–891 (2013).